Bioactive Materials 21 (2023) 97–109

Contents lists available at ScienceDirect

Bioactive Materials

journal homepage: www.keaipublishing.com/en/journals/bioactive-materials

Black phosphorus nanosheets-enabled DNA hydrogel integrating 3D-printed scaffold for promoting vascularized bone regeneration

Yali Miao [a,b], Yunhua Chen [a,b,c,*], Jinshui Luo [b], Xiao Liu [a,b], Qian Yang [b], Xuetao Shi [a,b,c,d,**], Yingjun Wang [a,b,c,d,***]

[a] School of Materials Science and Engineering, South China University of Technology, Guangzhou, 510641, China
[b] National Engineering Research Center for Tissue Restoration and Reconstruction, South China University of Technology, Guangzhou, 510006, China
[c] Key Laboratory of Biomedical Engineering of Guangdong Province, And Innovation Center for Tissue Restoration and Reconstruction, South China University of Technology, Guangzhou, 510006, China
[d] Key Laboratory of Biomedical Materials and Engineering of the Ministry of Education, South China University of Technology, Guangzhou, 510006, China

ARTICLE INFO

Keywords:
DNA hydrogels
3D-printed scaffold
Black phosphorus
Vascularized bone regeneration

ABSTRACT

The classical 3D-printed scaffolds have attracted enormous interests in bone regeneration due to the customized structural and mechanical adaptability to bone defects. However, the pristine scaffolds still suffer from the absence of dynamic and bioactive microenvironment that is analogous to natural extracellular matrix (ECM) to regulate cell behaviour and promote tissue regeneration. To address this challenge, we develop a black phosphorus nanosheets-enabled dynamic DNA hydrogel to integrate with 3D-printed scaffold to build a bioactive gel-scaffold construct to achieve enhanced angiogenesis and bone regeneration. The black phosphorus nanosheets reinforce the mechanical strength of dynamic self-healable hydrogel and endow the gel-scaffold construct with preserved protein binding to achieve sustainable delivery of growth factor. We further explore the effects of this activated construct on both human umbilical vein endothelial cells (HUVECs) and mesenchymal stem cells (MSCs) as well as in a critical-sized rat cranial defect model. The results confirm that the gel-scaffold construct is able to promote the growth of mature blood vessels as well as induce osteogenesis to promote new bone formation, indicating that the strategy of nano-enabled dynamic hydrogel integrated with 3D-printed scaffold holds great promise for bone tissue engineering.

1. Introduction

Craniofacial bone defects caused by various conditions, including degenerative diseases, trauma and cancer surgeries, face challenges in clinical treatment. In clinic, reconstructive operations are required to solve the skeletal injuries. Current approaches involve autologous grafts, allogenic grafts and alloplastic materials to improve the craniofacial bone repairing outcomes. However, the autologous and allogenic grafts have source limitation, while the alloplastic substitutes remain highly challenging to restore bone functions. Over the past decades, tissue engineering has provided a promising alternative approach for the regeneration of bone defects [1,2]. The *in vivo* regeneration of new bone critically depends on the coordination and guidance of distinct biological processes [3]. The scaffold, as one of the key elements of bone tissue engineering, could create a suitable spatial structure for cell growth and migration, which is essential for guiding bone regeneration. In this regard, 3D printing technology demonstrates great advantages and has been widely used to fabricate porous scaffolds with controllable shapes to adapt bone defects [4–6]. The classical 3D-printed scaffolds made from single biomaterials or composites [7], such as polycaprolactone (PCL), β-tricalcium phosphate and hydroxyapatite, demonstrate good mechanical strength approaching to natural bones. However, unlike the native extracellular matrix (ECM), the pristine 3D-printed scaffolds are often lack of inherent dynamic microenvironment with physical and chemical cues to direct cell behaviours. It would be appealing to endow the scaffolds with ECM-mimicking architecture

Peer review under responsibility of KeAi Communications Co., Ltd.
* Corresponding author. School of Materials Science and Engineering, South China University of Technology, Guangzhou, 510641, China.
** Corresponding author. School of Materials Science and Engineering, South China University of Technology, Guangzhou, 510641, China.
*** Corresponding author. School of Materials Science and Engineering, South China University of Technology, Guangzhou, 510641, China.
E-mail addresses: msyhchen@scut.edu.cn (Y. Chen), shxt@scut.edu.cn (X. Shi), imwangyj@scut.edu.cn (Y. Wang).

https://doi.org/10.1016/j.bioactmat.2022.08.005
Received 16 May 2022; Received in revised form 10 July 2022; Accepted 4 August 2022

and properties to promote bone regeneration.

Interestingly, the emergence of functional hydrogels provides plenty of possibilities to endow 3D printed scaffolds with hydrophilic network analogous to ECM [8–10]. Hydrogels demonstrate processability [11], and more remarkably, can be designed to adjust the key factors modulating bone regeneration, including growth factor delivery, mechanical stimulation, and cell-to-cell communication [12–18]. However, the properties of conventional chemical-crosslinking hydrogels are generally static, while cells within a tissue are subjected to dynamic micro-environment that determines their function and immunogenicity, variable physicochemical properties and fate [19,20]. Fortunately, hydrogels with dynamic properties can adapt to the environment, coordinate with the tissue regeneration process, and self-heal after damage [21–23]. The reversible network can be realized by dynamic covalent bonds or noncovalent interactions [24,25].

To this end, deoxyribonucleic acid (DNA), composed of monomeric nucleotides, is an interesting building block to prepare dynamic supramolecular hydrogels. DNA backbones treated with heating and cooling process can form a physical cross-linking network through multiple hydrogen bonds [26]. DNA hydrogel can serve as promising carrier to sustainably deliver active molecules including proteins and drugs. DNA hydrogel is injectable with shear thinning behaviour, while the mechanical strength is relatively weak. Remarkably, imparting nanoparticles to build nanocomposite network can effectively achieve mechanical reinforcement of DNA hydrogel [27]. Recent studies have shown the two-dimensional black phosphorus nanosheets (BPNSs) can form nano-enabled physical network with various polymers via noncovalent interactions [28]. Regarding to this, BPNSs could potentially bind with the macromolecular DNA strands, conferring functionality to the hydrogel while tightening the DNA cross-linking network. Specifically, BPNSs are biodegradable and have excellent biomineralization property [29] as well as osteoinductivity [30–32]. However, the current research on bone repair materials based on BPNSs has rarely considered the synergistic effect of angiogenesis on bone regeneration. It is well known that skeleton relies on the vascular system to maintain its metabolic balance, so vascularization is critical for bone regeneration and remodeling [33]. In mature bone, the vascular system provides the necessary signaling factors and nutrients to act as a communication bridge between bone and adjacent tissues [34]. The failure of implant materials to establish an effective vascular network can easily lead to the occurrence of local osteonecrosis. Therefore, developing bone implant materials with both angiogenic and osteogenic activities to accelerate the formation of vascular network in bone defect area is a feasible strategy to achieve material-guided high-efficiency bone regeneration. The high surface area of BPNSs and noncovalent interactions with bioactive molecules, such as electrostatic complexation, hydrophobicity and π-π stacking [35,36], probably ensure high loading efficiency and sustained release profile of bioactive molecules, such as vascular endothelial growth factor (VEGF). On account of these characteristics, imparting BPNSs nano-enabled DNA hydrogels with VEGF delivery would endow inert scaffolds with dynamic microenvironment and vascularization capabilities to enhance bone regeneration outcomes.

Herein, we engineered the dynamic DNA hydrogel with VEGF decorated BPNSs nanosheets and integrated with 3D-printed PCL scaffold to develop bioactive gel-scaffold construct for enhanced vascularized bone regeneration (Fig. 1). This nano-enabled strategy presented the advantage of developing reversible biological network without the need of chemical reaction or synthesis of specific DNA strand sequences. The structural and physical property analysis was applied to probe the BPNSs reinforcement effect. We evaluated the performance of nano-enabled hydrogel in modulating the release of VEGF as well as its biological activity. The gel-scaffold construct was further implanted in a rat cranial bone defect model to explore its performance on angiogenesis and bone regeneration. We envision that this gel-scaffold construct will offer great opportunity in promoting bone tissue regeneration where vascularization is critical.

2. Materials and methods

2.1. Preparation of BP/DNA hydrogel and gel-scaffold constructs

Liquid phase exfoliation method was used to prepare the black phosphorus nanosheets (BPNSs) [37,38]. First, the black phosphorus crystal powder (100944, Nanjing XFNANO Materials Tech Co., Ltd, China) was dispersed in ultrapure water. The mixture was sonicated for 9 h in an ice bath using a cell disruptor to obtain a brown dispersion. After that, the dispersion was sonicated in an ice bath for 4 h, and the supernatant was collected after centrifugation (10000 rpm) for 20 min.

To prepare nano-enabled hydrogels, 2.4 μg of VEGF (HEGFP-2265, Cyagen, USA) was added to 200 μL of BPNSs dispersion (600 ppm) and

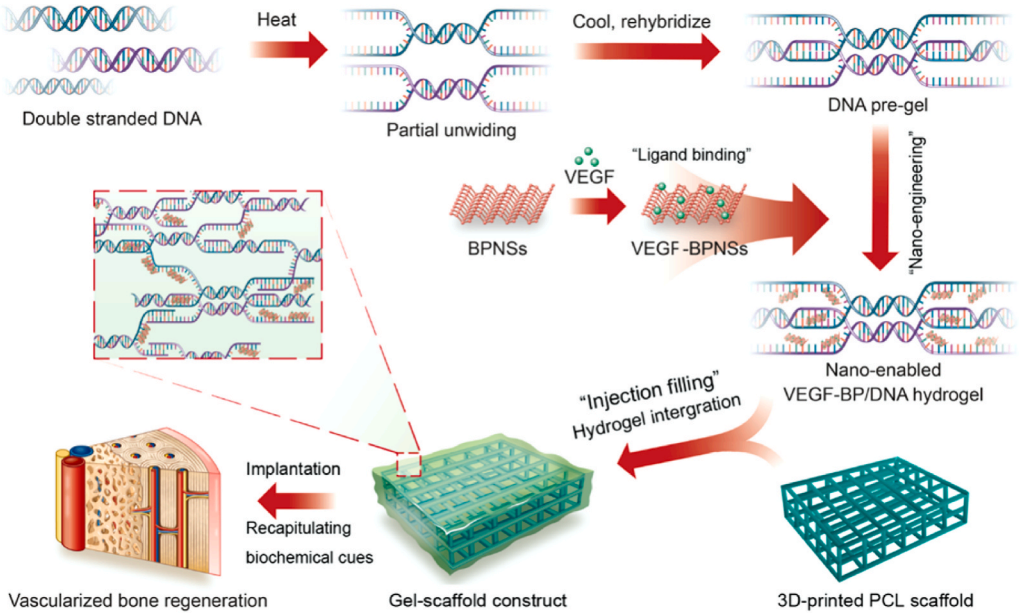

Fig. 1. Schematic illustration of the concept that integrating 3D-printed PCL scaffold and BPNSs-enabled DNA hydrogel loaded with VEGF for vascularized bone regeneration.

incubated at 4 °C for 12 h. DNA (deoxyribonucleic acid sodium salt from salmon testes, D1626, Sigma-Aldrich, USA, molecular weight ~1.3 × 10^6 g/mol, corresponding to ~2000 base pairs) was dissolved in DPBS at 40 °C for 12 h, after that, the DNA solution was pre-stirred in a 95 °C water bath for 5 min 200 μL of PBS, BPNSs dispersion (600 ppm) or VEGF-BPNSs dispersion (600 ppm) was added to 1 mL of 6 w/v% DNA pre-gel, respectively, and stirred until it was evenly dispersed in the pre-gel. These BP/DNA and VEGF-BP/DNA pre-gels were allowed to anneal for sufficient physical cross-linking at room temperature. To fabricate the gel-scaffold constructs, the nano-enabled hydrogels were directly injected into 3D-printed polycaprolactone scaffolds (PCL, 305048/305096, 3D Biotek, USA) at 40 °C and allow to anneal at room temperature without any further treatments.

2.2. Physical and structural characterization of BP/DNA hydrogels and the constructs

The average size and Zeta-potential of BPNSs and VEGF-BPNSs were measured by a Zetasizer instrument (Nano ZS90, Malvern, UK). For the sample preparation, 2 μL of VEGF solution (0.5 mg/mL) was added to 1 mL of 50 ppm BPNSs dispersion and incubated at 4 °C for 12 h. Transmission electron microscopy (TEM, JEM-2100HR, JEOL, Japan) and atomic force microscopy (AFM, MFP-3D-S, Asylum Research, USA) were used to characterize the morphology of BPNSs and VEGF-BPNSs. For the sample preparation of TEM testing, the grids supported carbon film were placed on filter paper, and 30 μL of dilute sample dispersion was dropped on the grids, following by drying in air at room temperature. AFM characterization was conducted in tapping mode (1 Hz scanning frequency).

Fourier infrared spectrophotometer (FTIR, CCR-1, Thermo Scientific, USA) was used to obtain the FTIR spectra of the hydrogel samples to analyze the interaction between BPNSs and DNA molecular chains in the hydrogel network. The morphology of the nano-enabled hydrogels coated with platinum was observed by using field-emission scanning electron microscopy (SEM, MERLIN, Zeiss, Germany) at an acceleration voltage ranging from 5 to 10 kV. The nano-enabled DNA hydrogels were also immersed into water with varied pH to investigate the stability against time.

The rheological analysis was performed by oscillating rheometer (MCR 302, Anton Paar, Austria). Strain sweep experiments were conducted to determine the linear viscoelastic response of hydrogels at 25 °C. Strain sweep experiments were performed with the amplitude varying from 0.1% to 2000% strain. Similarly, frequency sweep measurements were recorded from 0.01 Hz to 100 Hz. For the self-healing property measurements, continuous step change of oscillatory strain between 100% and 1% at 1 Hz was applied to test the strain-induced destruction and recovery of DNA/BP nano-enabled hydrogels.

The contact angles of PCL sheet and hydrogel-coated PCL sheets were measured by using a contact angle meter (DSA25, KRUSS, Germany). Measurements were carried out at least three times for each sample. The surface morphology of the PCL scaffold and gel-scaffold constructs was observed by SEM (Leica, Germany).

2.3. Cell culture

Rat bone marrow mesenchymal stem cells (BMSCs) were purchased from the Type Culture Collection of the Chinese Academy of Sciences (SCSP-402, Shanghai, China). BMSCs were cultured in Dulbecco's modified Eagle medium (DMEM, C11995500BT, Gibco, USA) containing 10% fetal bovine serum (Gibco, C2027050, USA) and 1% penicillin-streptomycin (Gibco, 15140-122, USA) at 37 °C under 5% CO_2. BMSCs were trypsinized and collected by centrifugation for passage and seeding. Human umbilical vein endothelial cells (HUVECs, 8000, Sciencell, USA) were cultured in endothelial cell basal medium (1001, Sciencell, USA). Other cell-culture ingredients were consistent with BMSCs.

2.4. The in vitro release of VEGF and its biological activity evaluation

The gel-scaffold construct was placed in a sterile Eppendorf tube without enzyme, and 2 mL of PBS solution containing 0.1% BSA was added. At the set time point, 200 μL of release medium was aspirated for VEGF content determination, and fresh 200 μL of PBS solution containing 0.1% BSA was supplemented to the Eppendorf tube. The released VEGF was quantitatively analyzed by using Human VEGF ELISA Kit (EK0470, SAB, USA). The cumulative release percentage of VEGF was calculated based on the values of concentration of released VEGF divided by the initial total concentration of VEGF encapsulated in hydrogels.

The bioactivity of VEGF released by the gel-scaffold constructs was determined by wound healing experiment. 1.0 × 10^5 HUVECs were seeded into Culture-Insert (80369, Ibidi, Germany) in a 24-well plate cultured with normal medium. After the HUVECs were overgrown, the Culture-Insert was gently removed with sterile forceps and the release medium was used to replace the normal medium. After the incubation for 12 h, HUVECs were fixed with 4% paraformaldehyde and stained with 0.1% crystal violet solution, and the scratch closure was observed by using an optical microscope. The migration rate of HUVECs was statistically analyzed by using ImageJ software. The total area of scratched surface was recorded as A_0, the area of scratched surface covered by HUVECs was recorded as A, and $A/A_0 \times 100\%$ was defined as the migration rate (n = 4).

2.5. Cell proliferation

The gel-scaffold constructs were immersed in the serum-free cell culture medium at a mass ratio of 50 mg/mL, and incubated in a shaker at 37 °C for 48 h to prepare the extract. The culture medium used for BMSCs was serum-free DMEM medium, and the culture medium used for HUVECs was serum-free endothelial cell basal medium, both of which contained 1% penicillin-streptomycin. The extracts were filtered with membrane filters (pore size 0.22 μm), and fetal bovine serum (HUVECs: 5 w/v%, BMSCs: 10 w/v%) was added to obtain the extract-containing medium for culturing cells.

2.6. In vitro angiogenesis

Briefly, 3 × 10^4 cells were seeded in each well of a 48-well plate. After cell adhesion, the extract-containing medium was introduced and the cells were cultured for 1, 3, and 5 days, respectively. For cell proliferation testing, CCK-8 working solution was prepared according to the volume ratio of fresh medium and CCK-8 stock solution (CK04-500T, Dojindo Laboratories, Japan) of 10:1, 200 μL of CCK-8 working solution was added to each well and incubated in cell incubator for 1 h. After that, 110 μL of incubation solution was pipetted into a 96-well plate and measured the absorbance at 450 nm with a microplate reader (Thermo 3001, Thermo Scientific, USA).

1 × 10^5 HUVECs were seeded in a 24-well plate. After culturing HUVECs in extract-containing medium for 3 days, quantitative RT-PCR analysis was performed to estimate the gene expression of several angiogenesis-related markers including VWF, CD31, and PDGF-B with GAPDH as the control gene. The specific primer sequences used were shown in Table 1 mRNA from the respective samples was extracted at day 3. Three different samples were tested for each group (n = 3). The ΔΔCt relative method was used to calculate the fold increase expression. The experimental results were normalized based on the gene expression levels obtained for HUVECs of the PCL scaffold group.

Immunofluorescence staining was used to analyze the secretion of VWF protein in HUVECs. HUVECs were seeded in a 24-well plate (1 × 10^5 cells/well) and cultured with different groups of extract-containing medium for 3 days, then VWF protein secreted by HUVECs was observed by Confocal Laser Scanning Microscopy (CLSM, Leica TCS SP8, Germany). The main steps were as follows: the HUVECs in the plate were

Table 1
Oligonucleotide primer sequences utilized for qRT-PCR.

Target DNA	Primer sequence (5′-3′)
GAPDH	F: TTGGCTACAGCAACAGGGTG
	R: TCTTCCTCTTGTGCTCTTGCTG
VWF	F: GGAAGTGCAGCAAGTGAGGC
	R: TATTGTGGGCTCAGAAGGGC
CD31	F: CCTCTGGGAACGCACGACT
	R: AGCACTTGGAAGGGGTCGC
PDGF-B	F: CTTGCGGCGTGTTCCTCT
	R: CAGGCCTGCGTGTATGTGC

fixed with 4% paraformaldehyde solution for 1 h at room temperature. After that, 0.1% Triton X-100 solution and 5% BSA solution were added into each well and incubated for 15 min and 1 h, respectively. Finally, HUVECs in the plate were incubated with Anti-Von Willebrand Factor antibody dilution (ab154193, Abcam, USA) for 12 h at 4 °C and Goat Anti-Rabbit IgG dilution (Alexa Fluor®647, ab150079, Abcam, USA) for 1 h at room temperature in dark, and the nuclei were labelled with DAPI dye solution (C1002, Cyagen, USA).

Subsequently, commercially available *in vitro* micro-angiogenesis orifices (81506, Ibidi, Germany) were used to characterize the tube formation of HUVECs. HUVECs were digested after being cultured with different groups of extract-containing medium for 3 days, and 1×10^4 HUVECs were seeded in the micro-angiogenesis well plate containing Matrigel (Corning, USA). After cultured in the endothelial cell basal medium for 6 h, the tube formation of HUVECs was observed by using an optical microscope. The formation of HUVECs tubes in the micro-angiogenesis well plate was observed under the bright field of an optical microscope. Then HUVECs in the micro-angiogenesis well plate were fixed with paraformaldehyde for 20 min and stained with Calcein-AM. Finally, HUVECs in the micro-angiogenesis well plate were photographed with a fluorescence microscope, and the number of tubes produced by HUVECs was counted by ImageJ software, and four images of different views were used for each sample.

2.7. In vitro osteogenic differentiation

1×10^5 BMSCs were seeded in 24-well plate. After cell adhesion, the extract-containing medium was added to culture BMSCs, quantitative RT-PCR was used to detect the expression of osteogenic related genes (Runx-2, ALP, OPN and OCN) with GAPDH as the control gene. The specific primer sequences used were shown in Table 2 mRNA from the respective samples was extracted at day 7 and day 14. Three different samples were tested for each group (n = 3). The ΔΔCt relative method was used to calculate the fold increase expression. The experimental results were normalized based on the gene expression levels obtained for BMSCs of the PCL scaffold group.

The formation of mineralized matrix was characterized by Alizarin Red staining after culturing BMSCs for 14 days with the extract-containing medium. BMSCs were firstly fixed with 4% paraformaldehyde, and then Alizarin Red solution was used to mark the mineralized matrix of BMSCs. After that, dodecylpyridine chloride solution (100 mM) was added to each well to quantify the amount of mineralized matrix. Finally, the absorbance at 562 nm was measured with a microplate reader (Thermo 3001, Thermo Scientific, USA).

Table 2
Oligonucleotide primer sequences utilized for qRT-PCR.

Target DNA	Primer sequence (5′-3′)
GAPDH	F: CACCCAGCCCAGCAAGGATA
	R: GCCCCTCCTGTTGTTATGG
Runx-2	F: TCCTTCCCTCCGAGACCCTA
	R: GGTCAGTCAGTGCCTTTCCTT
ALP	F: GCCAGGCTGGGAAGAACAAC
	R: ACAGGGGAGTCGCTTCAGTG
OPN	F: GGCCCTGAGCTTAGTTCGTTG
	R: GCAGTGGCCATTTGCATTTC
OCN	F: GGCGCTACCTCAACAATGGAC
	R: CGTCCTGGAAGCCAATGTG

2.8. In vivo angiogenesis and osteogenesis performance

The animal procedures were performed in accordance with the Guidelines for Care and Use of Laboratory Animals of South China University of Technology and approved by the University Animal Ethics Committee. The *in vivo* bone repair performance of the gel-scaffold construct was evaluated in the Sprague-Dawley rat (6 weeks, female) cranial defect model. Twenty-seven rats were used and two 5 mm-diameter bone defects were created in each rat for material implantation, with five samples per group at different time points. The bone defects without implanted materials were regarded as the blank group. At time frame of 4 and 8 weeks, the Sprague Dawley rats were sacrificed and their craniums were subjected to Micro-CT analysis (Explore Locus SP, GE, USA). ZKKS-MicroCT4.1 software was used to calculate the relevant bone parameters.

To observe the tissue morphology of new bones, the cranium tissue was fixed in 4% formalin, decalcified, and embedded in paraffin to prepare tissue sections. Then H&E, Masson staining, and immunohistochemistry were performed. For immunofluorescence staining, the slices were processed sequentially with EDTA antigen retrieval buffer (pH 9.0) and BSA solution, and anti-CD31 Mouse mAb (GB12063, Servicebio, China) or anti-osteocalcin antibody (ab13418, Abcam, USA) was added to the slices and incubated at 4 °C for 12 h. Then Cy3 conjugated goat anti-mouse IgG (GB21301, Servicebio, China) or HRP conjugated goat anti-mouse IgG (GB23301, Servicebio, China) was dropped on the section and incubated at room temperature for 50 min. Finally, the nuclei were stained with DAPI, and the digital pathology scanning system (P250 FLASH, 3DHISCETH, Hungary) was used for observation.

2.9. Statistical analysis

All data were expressed as means ± standard deviation (SD) and were analyzed using one-way ANOVA with a post hoc test. A p-value < 0.05 was considered statistically significant. $^*p < 0.05$, $^{**}p < 0.01$, $^{***}p < 0.001$.

3. Results and discussion

3.1. Preparation of nano-enabled DNA supramolecular hydrogels

In this study, DNA was used as the building blocks to prepare nano-enabled physical hydrogels. Black phosphorus nanosheets (BPNSs) were imparted into the DNA hydrogels to assist the formation of dynamic polymer network. The BPNSs were synthesized by liquid phase stripping from black phosphorus powder. The scanning electron microscopy (SEM) and transmission electron microscopy (TEM) images revealed the two-dimensional structure of BPNSs, and the average lateral size of BPNSs was approximately 200 nm (Fig. 2a and b). The high-resolution TEM image showed the good crystallinity of BPNSs, where lattice fringes of 0.24 nm assigned to the crystal plane of orthorhombic phosphorus can be observed. The selected-area electron diffraction (SAED) also confirmed the preservation of crystalline features of BPNSs during exfoliation procedure.

The BPNSs were dispersed in deionized water to form homogeneous dispersion. Thereafter, the aqueous BPNSs dispersion was then added into DNA hydrogel followed by vortex mixing to produce nano-enabled DNA hydrogel (Fig. 2c). The interactions were detected by testing the hydrogel viscosity as a function of shear rate ranging from 0.01 to 100 s^{-1}. Since BPNSs were imparted into the DNA hydrogel matrix, a corresponding increase in viscosity was demonstrated (Fig. 2d). Also, the

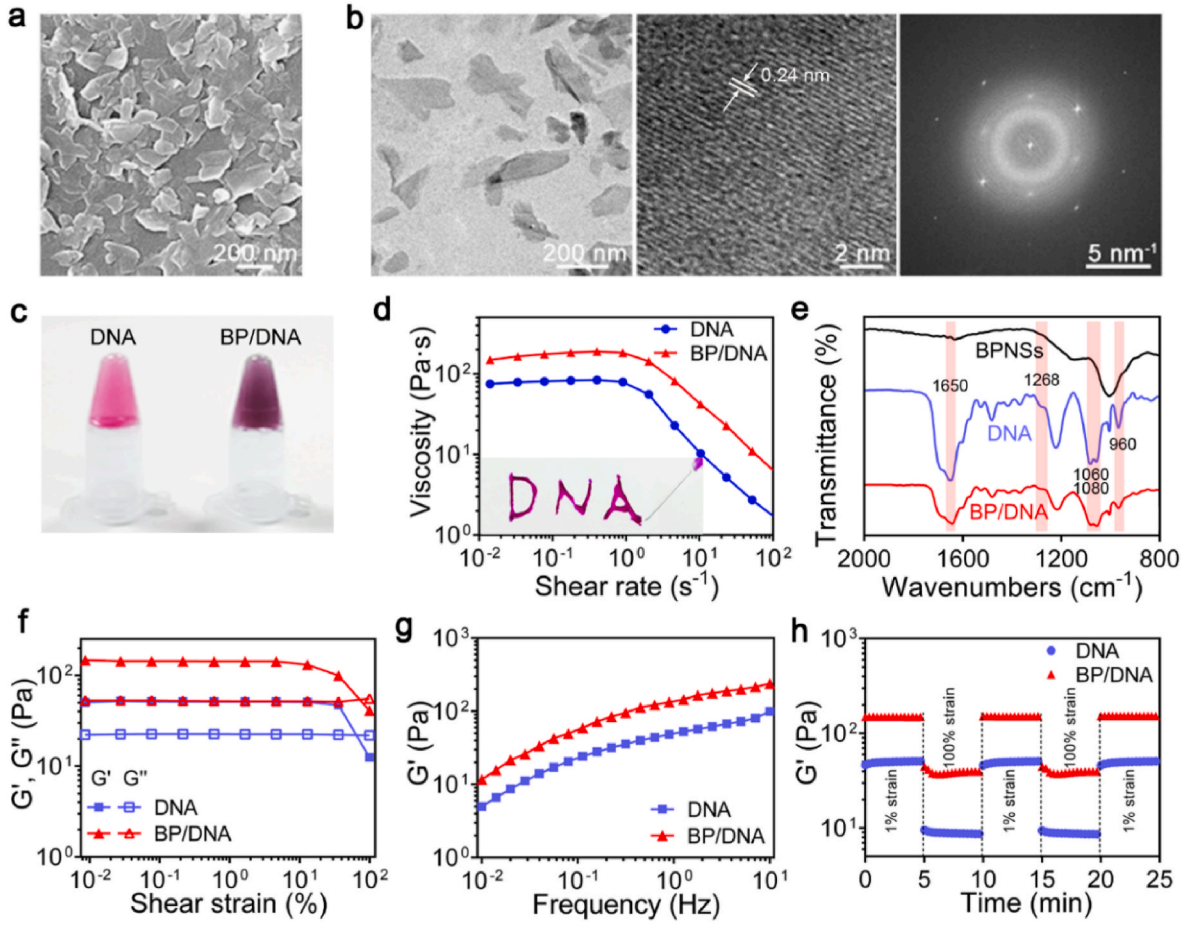

Fig. 2. Physical properties of BPNSs-enabled DNA supramolecular hydrogel. (a) SEM image of exfoliated BPNSs. (b) TEM images of BPNSs, left: topographic image, middle: high resolution image, right: SAED image. (c) Photograph of BPNSs-enabled DNA hydrogel. (d) Viscosity vs shear rate plots demonstrated an increase in the viscosity of BP/DNA hydrogel due to the presence of BPNSs. The physical hydrogels showed shear-thinning behaviour. (e) FTIR spectra of BPNSs, DNA and BP/DNA hydrogels, showing the physical interaction between BPNSs and DNA. (f) Strain sweep measurement of hydrogels: the change of the storage and loss moduli indicated the linear viscoelastic region at 0.01%–10%. (g) Frequency sweep measurement in the range of 0.01–10 Hz, showing the BPNSs enhanced storage modulus of BP/DNA hydrogel. (h) Mechanical recovery of hydrogels as determined by the change of storage modulus under alternating high (100%) and low strain (1%).

increase in shear rate clearly led to the viscosity decrease, showing the shear thinning nature of this nano-enable DNA hydrogel, which is essential for injectable hydrogels. To further identify the interactions between BPNSs and the DNA molecular chains, FTIR characterization was carried out on the hydrogels with and without BPNSs (Fig. 2e). Pristine DNA hydrogel exhibited the C–O stretching vibration peak of the sugar ring at 1268 cm^{-1} and the O–P–O bending vibration peak at 960 cm^{-1}, corresponding to the structural characteristic peaks of DNA. After the introduction of BPNSs, the carbonyl vibration peak at 1650 cm^{-1} of the DNA base shifted to a lower wave number due to the physical interactions between BPNSs and the DNA backbone. In addition, the intensity of peak at 960 cm^{-1} corresponding to the O–P–O bending vibration was weakened, and the shape and intensity of the C–O characteristic peaks of DNA molecules at 1060 cm^{-1} and 1080 cm^{-1} had changed significantly. This finding indicated the changes of DNA molecular environment and the existence of interactions between BPNSs and DNA backbone.

Oscillatory rheological analysis was then performed to investigate the effect of BPNSs on the mechanical properties of the nano-enabled DNA hydrogel. The linear viscoelastic region of hydrogel was determined by detecting the change of storage modulus (G′) and loss modulus (G") as a function of shear strain. In the strain range of 0.01%–10%, both G′ and G″ of DNA and BP/DNA hydrogels were constant with the values of G′ higher than G'' (Fig. 2f). Subsequently, frequency sweep measurement was conducted in the linear viscoelastic region at frequencies ranging from 0.01 to 10 Hz. It can be found that the introduction of BPNSs can significantly increase the storage modulus of DNA hydrogel (Fig. 2g). When designing an injectable nano-enabled hydrogel, it is important that the material can withstand cyclic strain and quickly restore its original structure as well as mechanical strength after removing the shear stress. Oscillation strain amplitude test was performed by applying high strain (100%) and low strain (1%) to observe the change of storage modulus. As shown in Fig. 2h, subjected to several cycles of strain variation, the complete recovery of storage moduli within seconds can be observed in both DNA and BP/DNA hydrogels, indicating the self-healing capability of the physical crosslinking network. These results might be attributed to the physical interactions including π-π stacking between the six-membered ring of BPNSs and the DNA backbone. These interactions regulated the mechanical stability of BP/DNA hydrogel, and the formation of the additional cross-linking points can be responsible for the observed increase in the G' value.

In addition, we investigated the internal structure of the nano-enabled DNA hydrogel since this parameter is related to crosslinking density and could affect the release profile of encapsulated payloads. As shown in Fig. 3a, the introduction of BPNSs clearly resulted in a decrease of pore size of hydrogel, indicating the formation of a denser nanocomposite network with a higher degree of physical crosslinking. BPNSs were embedded in the physical crosslinking network, which could be beneficial to their stability maintenance as well as retardant degradation in the physiological environment. It was interesting to note that the

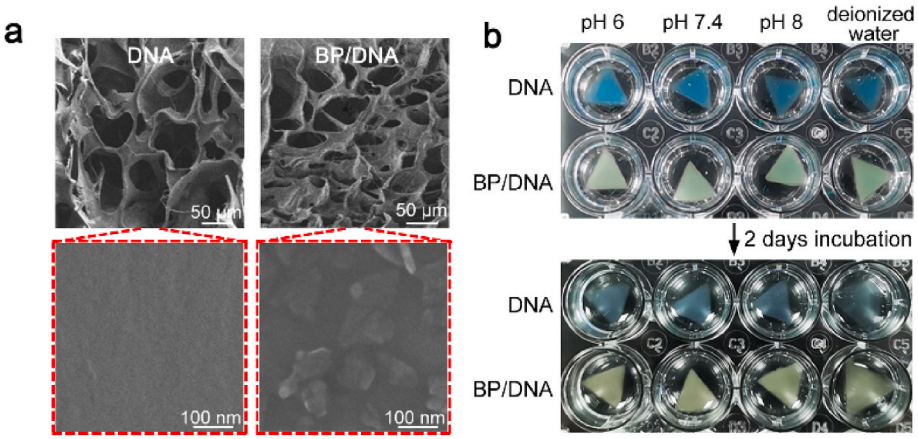

Fig. 3. Morphology and volume stability of BP/DNA nano-enabled hydrogel. (a) SEM images of BP/DNA hydrogel showing the reduced pore size of lyophilized matrix in the presence of BPNSs. (b) Stability of DNA and BP/DNA hydrogels in deionized water and PBS at different pH values.

dimension of DNA and BP/DNA hydrogels had no obvious changes in PBS buffer solution, showing insignificant swelling after 2 days of incubation at 37 °C (Fig. 3b). Overall, these findings demonstrated the great capability of BPNSs in the modulation of structural and physical properties using an ultra-low particle concentration as compared to other nanocomposite hydrogels. This is a great advantage since a lower concentration of nano-structured materials in hydrogels is beneficial to reduce their possible cytotoxicity.

3.2. VEGF binding onto BPNSs

BPNSs have high specific surface area and folded lattice structure, which are conducive to drug loading and multi-modal collaborative treatment [39–41]. We firstly studied the binding situation between BPNSs and VEGF by using TEM. BPNSs and VEGF were co-incubated to produce VEGF-BPNSs sample, dotted surface morphology can be clearly observed comparing to pristine BPNSs, as shown in Fig. 4a. We conjectured that the nanoparticles/dots on the surface of BPNSs attribute to VEGF as the inset TEM image of VEGF showed similar morphology. Further analysis of the surface elements of VEGF-BPNSs clearly revealed that C, N, and O elements were distributed on the surface of BPNSs (Fig. 4b), indicating VEGF binding onto BPNSs successfully. To quantitatively analyze the thickness distribution of the nanosheets, we randomly selected two linear regions of AFM images. As shown in

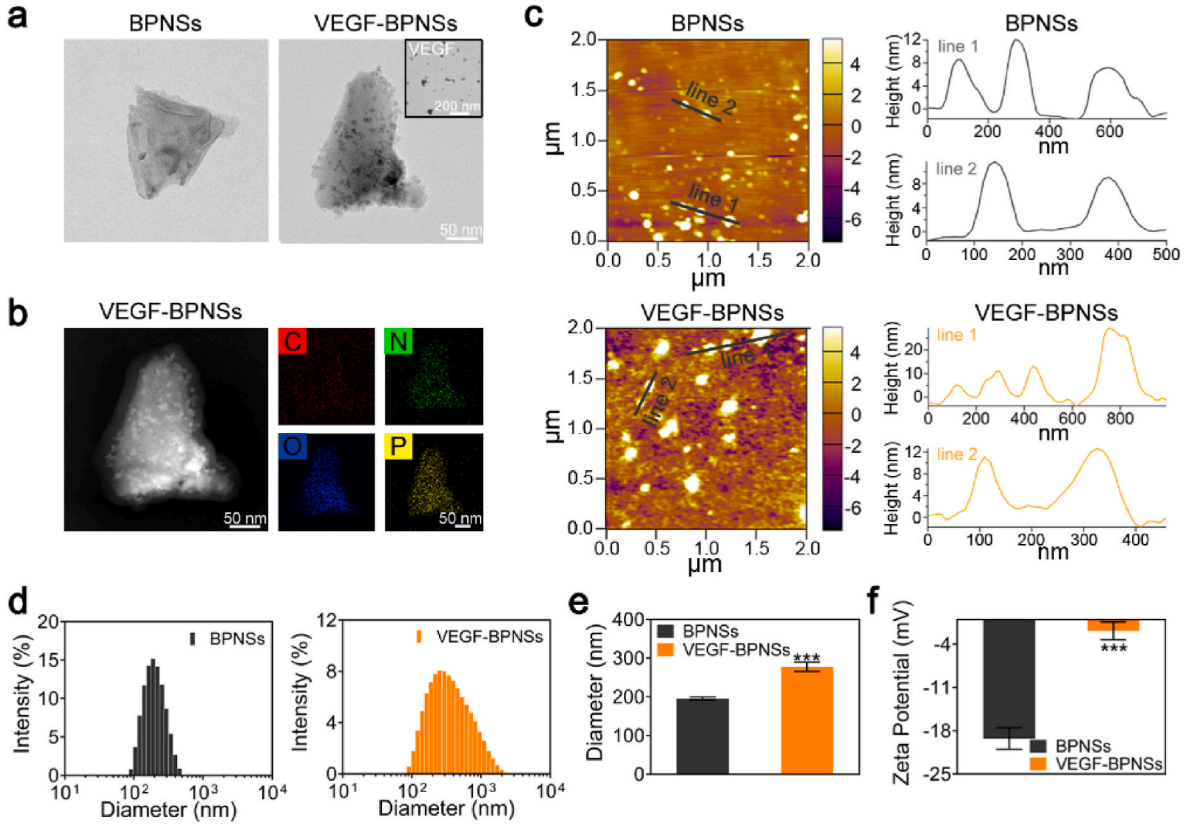

Fig. 4. The physical binding of VEGF onto BPNSs. (a) TEM images of BPNSs and VEGF-BPNSs. (b) Topography and surface element analysis demonstrated that VEGF can be physically adsorbed on the surface of BPNSs. (c) AFM images of BPNSs and VEGF-BPNSs, the height profile showed the increased thickness of VEGF-BPNSs. (d) Particle size distribution, (e) Average size and (f) Zeta potential of BPNSs and VEGF-BPNSs. $^{*}p < 0.05$, $^{**}p < 0.01$, $^{***}p < 0.001$.

Fig. 4c, the thickness of the VEGF-BPNSs was ranging from 10 nm to 25 nm, which was higher than that of pristine BPNSs (8–12 nm), due to the VEGF adsorbed on the surface of BPNSs.

Dynamic light scattering (DLS) and Zeta-potential analysis were then used to study the size and surface potential variation of BPNSs with/without VEGF binding. As shown in Fig. 4d–f, after incubation with VEGF, the particle size of BPNSs increased sharply from 196 ± 4 nm to 277 ± 12 nm, while the surface potential increased from −19 ± 2 mV to −2 ± 2 mV, confirming the non-covalent interaction between BPNSs and VEGF. Due to the random absorption of VEGF onto BPNSs, the size distribution of VEGF-BPNSs was relatively wide. It is known that the isoelectric point of VEGF is 8.5, and VEGF has a positive charge at neutral pH [42], while BPNSs have a negative surface charge with a layer gap about 5.24 Å [43]. VEGF can be adsorbed on the surface of BPNSs or embedded in the interlayer space through electrostatic interaction, resulting in a decrease in the negative charge density and an increase in the particle size of BPNSs. Therefore, these results suggested the non-covalent binding of VEGF onto BPNSs.

3.3. Gel-scaffold construct and VEGF delivery

In the physiological environment, growth factor VEGF is easily degraded to lose its bioactivity. Encapsulating VEGF with biomaterials can not only retain its activity, but also realize the sustainable release of VEGF at a specific defect site. The nano-enabled injectable BP/DNA hydrogel could serve as a promising VEGF delivery carrier and biological coating to activate inert implants. To verify our hypothesis, VEGF-BPNSs were physically embedded in the DNA physical network and then imparted into a 3D-printed PCL scaffold through direct injection to build a gel-scaffold construct. The pristine DNA hydrogel, BP/DNA hydrogel and VEGF-BP/DNA hydrogel coated PCL scaffolds were named as DNA + PCL, BP/DNA + PCL and VEGF-BP/DNA + PCL, respectively.

As shown in Fig. 5a, it can be found that the PCL scaffold appeared a relatively regular porous structure with an average pore size of 500 μm, and the diameter of filaments was about 300 μm. DNA and BP/DNA hydrogels were homogeneously filled into the scaffolds, and the loaded VEGF had insignificant influence on the network structure of BP/DNA hydrogel. The analogue extracellular matrix and proper hydrophilic surface of implant materials could be beneficial to cell growth [44]. The average contact angle of the PCL sheet was 77.7°, presenting a relatively hydrophobic surface. However, the average contact angles of the PCL sheets coated with DNA, BP/DNA and VEGF-BP/DNA hydrogels decreased to 39.0°, 38.5°and 36.6°, respectively (Fig. 5b and c). This finding revealed that the DNA-based hydrogels can effectively wet PCL scaffolds.

We monitored the release of VEGF from the gel-scaffold constructs over a period of 6 days (Fig. 5d). In the initial two days, VEGF diffused rapidly and showed a burst release from the VEGF-DNA + PCL construct, while the VEGF-BP/DNA + PCL construct demonstrated a much slower release behaviour. The release rate of VEGF gradually decreased and stabilized with time afterwards. On the 6th day, the cumulative release of VEGF in VEGF-DNA + PCL construct was close to 95% of the total VEGF loading, which was much higher than that of VEGF in the VEGF-BP/DNA + PCL construct, implying enhanced retention of VEGF in the hydrogel containing BPNSs. It can be explained that the high permeability and weak internal cross-linking network of pristine DNA hydrogel led to the rapid release of VEGF. On the contrary, the relatively compact crosslinking network in the BP/DNA + PCL construct hindered the rapid diffusion of VEGF, and the interactions between BPNSs and VEGF also contributed to the long-term retention of VEGF.

It is important to confirm that the VEGF released from VEGF-BP/DNA + PCL construct still retained its biological activity. The migration ability of HUVECs was often regarded as an index to evaluate the bioactivity of VEGF. The wound healing experiment was used to assess the migration behaviour of HUVECs (Fig. 5e). Scratch area formed by HUVECs was regular with a gap of 500 μm, ensuring that the initial state between groups was consistent. After culturing HUVECs with the extract-containing medium for 12 h, HUVECs of VEGF-BP/DNA + PCL construct significantly promoted the migration of HUVECs to the middle of the scratch, which was similar to the cell migration observed in the VEGF group. Specifically, HUVECs of the VEGF-BP/DNA + PCL construct covered 54% of the total scratch area, HUVECs of the blank group only covered 30% of the scratched area (Fig. 5f). It was worth noting that the amount of cell migration in the VEGF-DNA + PCL and VEGF-BP/DNA + PCL groups was higher than that in the VEGF group, which may be due to the higher concentration of VEGF contained in the extraction solutions of these two groups than that in the VEGF group (20 ng/mL). The above results clearly suggested that the VEGF released from the VEGF-BP/DNA + PCL construct could stimulate the migration of HUVECs, confirming that the released VEGF retained its biological activity.

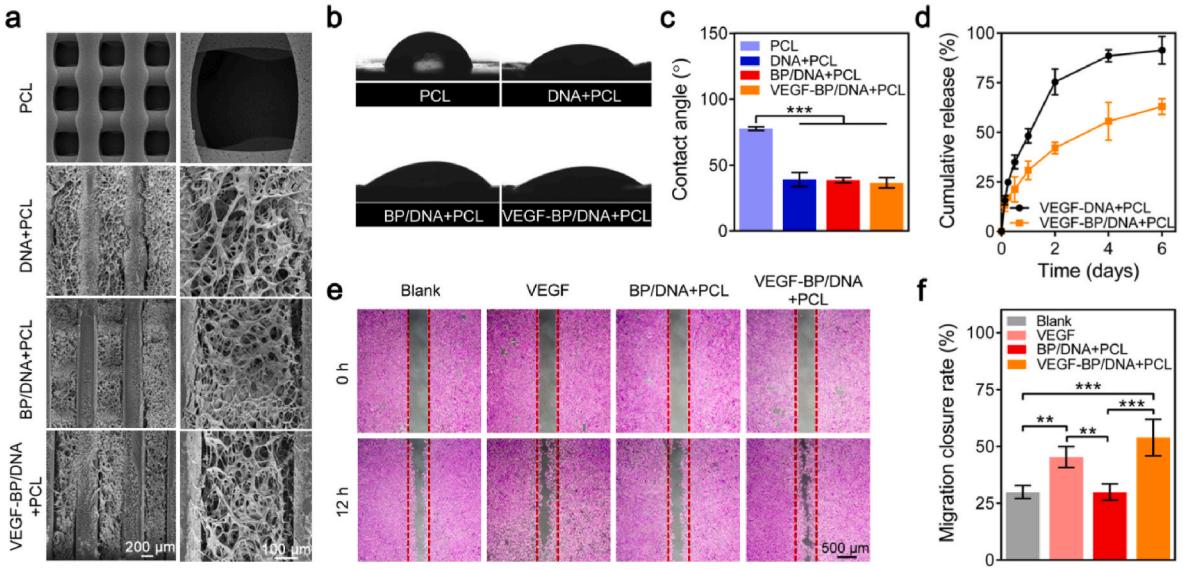

Fig. 5. The morphology and VEGF delivery of gel-scaffold constructs. (a) SEM images of gel-scaffold constructs. (b) Water droplets and (c) contact angles on the PCL sheet and hydrogel-coated PCL sheets. (d) The release profiles of VEGF from the gel-scaffold constructs. (e) The stimulation effect of released VEGF on HUVECs migration. (f) HUVECs migration closure rate of the scratch after 12 h $^{*}p < 0.05$, $^{**}p < 0.01$, $^{***}p < 0.001$.

3.4. Gel-scaffold construct enhances in vitro angiogenesis

The cytocompatibility of gel-scaffold constructs was evaluated by performing CCK-8 assay. As shown in Fig. 6a, all samples had negligible influence on HUVECs viability, and remarkably, the BP/DNA + PCL construct loaded with VEGF can effectively promote the proliferation of HUVECs. This result revealed the good cytocompatibility of the gel-scaffolds and the positive regulation of HUVECs growth behaviour by VEGF.

Adequate vascularization is essential for bone defect repair. The influence of gel-scaffold construct on cellular angiogenesis was then compressively studied over a period of 3 days. In this study, the angiogenesis-related genes VWF, CD31 and PDGF-B were selected as HUVECs angiogenesis marker genes to evaluate the angiogenic performance of HUVECs *in vitro*. As shown in Fig. 6b, the expression of VWF, CD31 and PDGF-B genes of HUVECs in the VEGF-BP/DNA + PCL construct group was significantly up-regulated compared to other groups, which may be attributed to the effect of released VEGF. We further performed immunofluorescence staining on the VWF protein of HUVECs. As shown in Fig. 6c, the nuclei of HUVECs were stained blue, and VWF protein secreted by HUVECs was stained red. HUVECs in all groups could secrete VWF protein distributed in the extracellular matrix. HUVECs of construct showed significantly larger area of red fluorescence, especially HUVECs of VEGF-BP/DNA + PCL construct, indicating that more VWF protein was secreted. The combination of the bioactive hydrogel matrix and the porous scaffold provided a matrix environment that was more conducive to the angiogenesis of HUVECs, and the loading of VEGF can significantly up-regulate the angiogenic markers expression of HUVECs, thereby promoting the angiogenesis of HUVECs.

We further evaluated the effect of gel-scaffold constructs on tube formation ability of HUVECs *in vitro* (Fig. 6d). HUVECs of the PCL scaffold and VEGF-free constructs presented a scattered distribution. In contrast, the majority of HUVECs in VEGF-BP/DNA + PCL construct participated in the formation of tubes, thus there was a significant improvement on the ability of tube formation. To observe the formation of tubes more clearly, HUVECs were labelled with green fluorescence (Fig. 6e). The number of tubes formed by HUVECs of PCL scaffold, DNA + PCL, BP/DNA + PCL and VEGF-BP/DNA + PCL constructs were 8, 9, 12 and 33, respectively (Fig. 6f), indicating that VEGF-BP/DNA + PCL construct can significantly promote the tube formation performance of HUVECs *in vitro*.

3.5. Gel-scaffold construct promotes in vitro osteogenic differentiation

The effect of gel-scaffold constructs on the cell proliferation was evaluated by CCK-8 assay using bone mesenchymal stem cells (BMSCs). As shown in Fig. 7a, on the first day, there was no obvious difference in cell viability between the pristine PCL scaffold and gel-scaffold constructs. With increasing cultivation time, the nano-enabled DNA gel-scaffold constructs can significantly promote the proliferation of BMSCs compared to the PCL scaffold, which could attribute to the synergistic effect of VEGF and BPNSs on BMSCs growth.

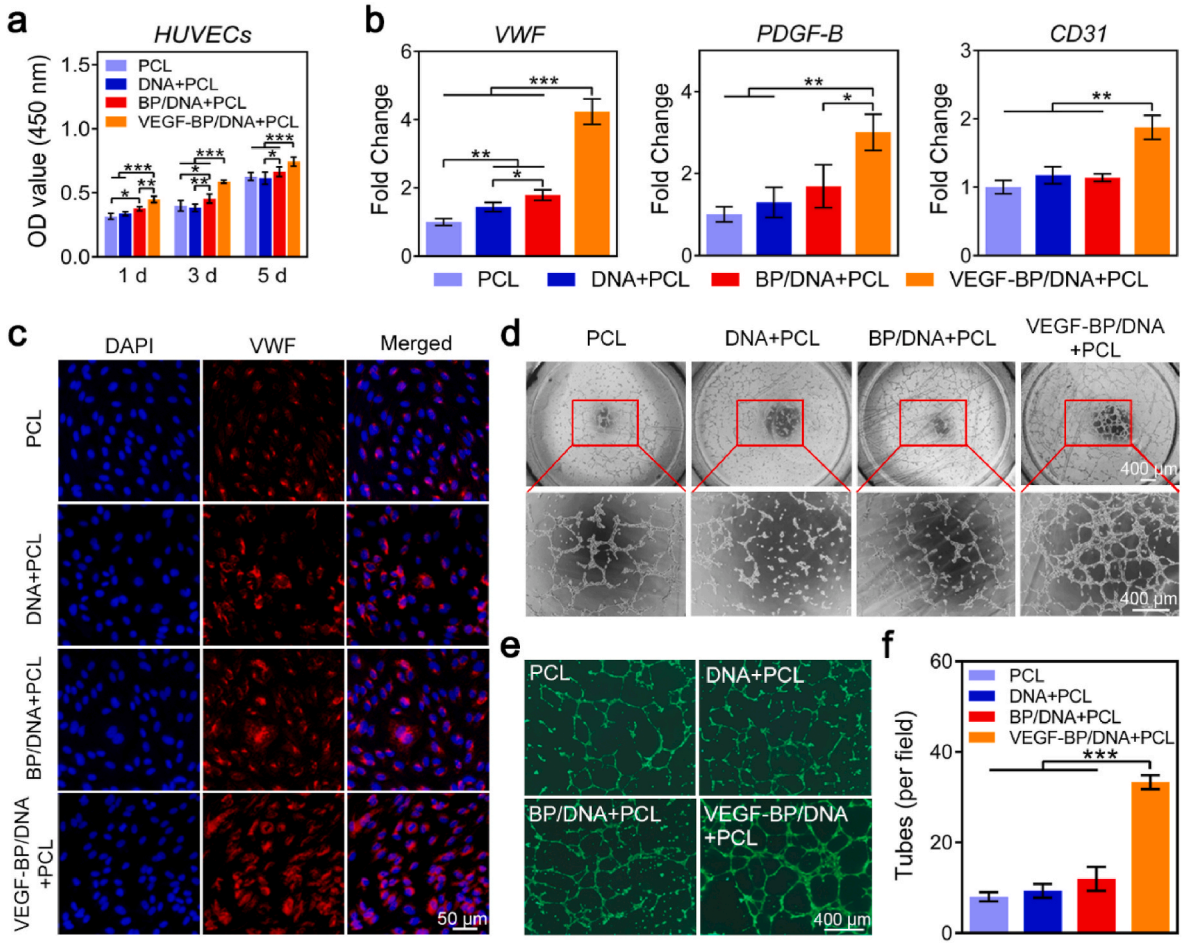

Fig. 6. Effect of gel-scaffold constructs on angiogenesis of HUVECs. (a) The viability of HUVECs treated with the extracts of gel-scaffold constructs for 1, 3 and 5 days. (b) mRNA expression of angiogenesis-related genes (VWF, CD31 and PDGF-B) of HUVECs cultured for 3 days. (c) Immunofluorescence images of HUVECs, the red fluorescent area represented the VWF protein, and the blue fluorescent area represented the nuclei. (d) Bright-field optical microscopy observation of tube formation of HUVECs. (e) Fluorescence images of HUVECs stained with Calcein-AM. (f) Number of tubes formed by HUVECs. $^{*}p < 0.05$, $^{**}p < 0.01$, $^{***}p < 0.001$.

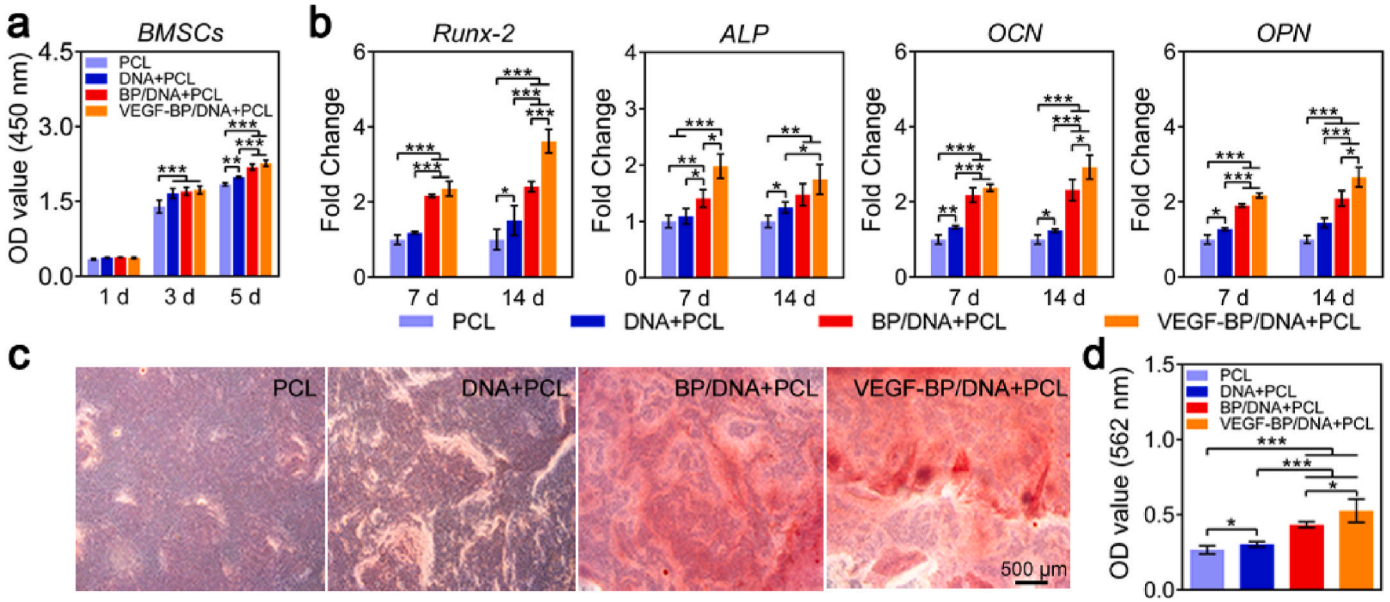

Fig. 7. Effect of gel-scaffold constructs on osteogenic differentiation of BMSCs. (a) The viability of BMSCs treated with the extracts of gel-scaffold constructs for 1, 3 and 5 days. (b) mRNA expression of osteogenic-related genes (Runx-2, ALP, OCN and OPN) of BMSCs cultured for 7 and 14 days. (c) Mineralized matrix stained by Alizarin Red after BMSCs were treated with the extracts for 14 days. (d) OD values of the mineralized matrix measured at a wavelength of 562 nm for quantitative analysis. $^{*}p < 0.05$, $^{**}p < 0.01$, $^{***}p < 0.001$.

The characteristic physical and biochemical cues of extracellular matrix (ECM) are important in regulating stem cell function and fate [45,46]. It is also possible to realize enhanced outcomes of tissue regeneration by regulating these ECM cues. In this study, the effect of nano-enabled DNA hydrogel on osteogenic responses of BMSCs were investigated by qualitative and quantitative evaluation of the activity of key marker genes of differentiation at day 7 and day 14. As shown in Fig. 7b, BMSCs of four groups all expressed the selected osteogenic-related marker genes, including Runx-2, ALP, OCN and OPN. The expression of ALP gene in the constructs was significantly higher than that in the PCL scaffold, indicating that the extracellular matrix-like environment of hydrogels effectively stimulated the expression of ALP. Different from the ALP, the combination of VEGF and BPNSs can synergistically promote the expression of Runx-2, resulting in the expression of Runx-2 in the VEGF-BP/DNA + PCL construct being significantly higher than that in other groups. In the late stage of osteogenic differentiation, the expression of OCN in the VEGF-BP/DNA + PCL construct was 2.9 times higher than that in the PCL scaffold. These results clearly demonstrated that the incorporated BPNSs and VEGF in the nano-enabled DNA hydrogel had a significant synergistic effect on accelerating the osteogenic differentiation process of BMSCs.

In the physiological process of bone mineralization, the deposition of calcium phosphate crystals in the extracellular matrix occurs, which is essential for the process of bone regeneration and bone remodeling. The mineralized matrix produced by BMSCs was marked in red by Alizarin Red staining, as shown in Fig. 7c. The constructs containing BPNSs provided a favourable matrix environment for the formation of mineralized matrix. Moreover, the loaded VEGF significantly enhanced the positive regulation of BPNSs on the osteogenic differentiation of BMSCs (Fig. 7d). Overall, in the absence of osteogenic growth factors, the formation of the mineralized matrix was mainly regulated by VEGF and BPNSs in the construct, thereby endowing the gel-scaffold construct with excellent osteoinductivity.

3.6. *In vivo* bone regeneration of nano-enabled gel-scaffold constructs

Finally, we assessed the bone regeneration potential of the gel-scaffold construct in a rat cranial defect model, procedure and timeline of *in vivo* implantation as shown in Fig. 8a. Microcomputed tomography (Micro-CT) reconstruction was performed on the bone defect site to assess cranium regeneration (Fig. 8b). The new bone mainly grew from the edge of defect toward the center and deposited along the direction of the scaffold filaments. Meanwhile, there was no obvious newly formed bone in the defect of blank group. On the contrary, the PCL scaffold and the gel-scaffold constructs with suitable osteoconductivity promoted the growth of new bone. The VEGF-BP/DNA + PCL construct demonstrated a superior capacity for cranial defect regeneration compared to other constructs, confirming that the BPNSs with VEGF angiogenesis ability exhibited outstanding performance for bone repair. The parameters related to new bone formation were shown in Fig. 8c. The highest bone formation percentage and density of new bone were observed in the VEGF-BP/DNA + PCL construct, indicating that BPNSs and VEGF provided an appropriate environment for bone regeneration.

Hematoxylin and eosin (H&E) staining was used to evaluate the formation of new bone within the defect (Fig. 8d). There was a lot of fibrous tissue without newly bone formed in the bone defect of blank group. After the gel-scaffold construct was implanted, the hydrogel matrix inside the scaffold gradually degraded, resulting in the exposure of the porous structure. Due to the limited bone regeneration ability of the PCL scaffold and the DNA + PCL construct, there was only a little amount of new bone in the bone defect. On the contrary, the nano-enabled gel-scaffold constructs were more tightly bound to the host bone, and a large amount of new bone can be clearly observed in the bone defect area of the VEGF-BP/DNA + PCL construct, revealing its enhanced osseointegration.

Masson staining was used to stain the collagen fibers to further assess the bone formation and bone maturity. The new and mature bone matrix were shown in blue and red after staining, respectively. The structural characteristics in Fig. 9a exhibited that the bone matrix in the VEGF-BP/DNA + PCL construct showed the best structural integrity among all the groups. The regenerated bone was well bonded to the adjacent host bone in the nano-enabled gel-scaffold constructs, and VEGF associated with BPNSs can synergistically promote the formation and maturation of bone matrix. It was worth noting that there was obvious micro-vessel formation at the 4th week, while the number of micro-vessels

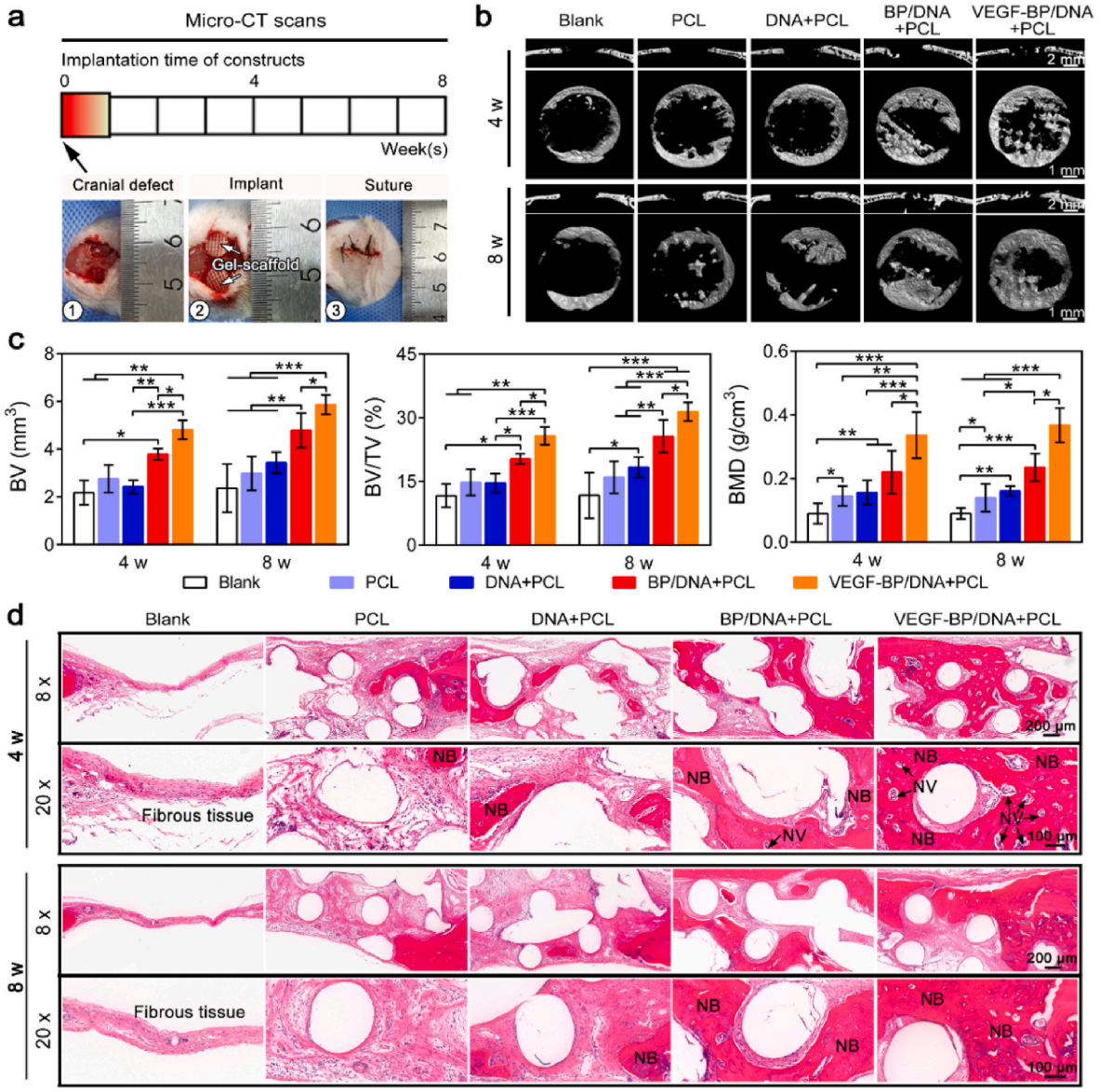

Fig. 8. *In vivo* bone defect repair facilitated by the gel-scaffold constructs. (a) Procedure and timeline of gel-scaffold construct implantation. (b) Micro-CT images of cranial defects treated with constructs, including cross-sections and longitudinal sections. (c) Quantitative analysis of osteogenesis-related parameters, BV represented the volume of new bone, TV represented the total volume of the defect and BMD represented the density of new bone. (d) H&E staining images of cranial defects after the implantation of gel-scaffold constructs for 4 and 8 weeks, NV indicated by the arrow represented for new blood vessels, and NB represented new bone tissue. $^{*}p < 0.05$, $^{**}p < 0.01$, $^{***}p < 0.001$.

decreased at the 8th week. The possible reason was that the micro-vessels formed by the differentiation of native cells inside the VEGF-BP/DNA gel-scaffold construct cannot effectively integrate with the blood vessels of the surrounding tissue, making the micro-vessels regress, leaving only part of the micro-vessels that grew into the scaffold from the surrounding tissue. Taken together, we speculated that both forms of vascularization including vascularization of native tissue growing into the construct and vascularization of native cell differentiation occurred.

After further analysis of OCN immunohistochemical sections (Fig. 9b), it was found that the expression of OCN marker of gel-scaffold constructs containing BPNSs was more significant, that is, the yellow-brown positive expression area, indicating that BPNSs in the constructs can effectively enhance the deposition of the bone mineralized matrix. By analyzing the CD31 immunofluorescence and immunohistochemical staining images (Fig. 9b–d), it demonstrated that the CD31 positive expression area of VEGF-BP/DNA + PCL construct around the new bone matrix was significantly more than that of the blank group, PCL scaffold, DNA + PCL and BP/DNA + PCL constructs, and the new tissue of the VEGF-BP/DNA + PCL construct had more capillary structures with obvious erythrocytes inside compared with other groups, suggesting the formation of early blood vessels and enhanced vascularized bone regeneration.

Overall, the *in vivo* bone defect model results demonstrate the exciting possibility of VEGF-BP/DNA hydrogel as filling and repairing biomaterial for irregular non-load-bearing bone defect repair. Although the mechanical strength of VEGF-BP/DNA hydrogel is weak comparing to metal or inorganic scaffolds, it could serve as bioactive matrix in combination with high-strength porous scaffold for load-bearing bone regeneration. Also, it should be noted that functionalized hydrogel materials for treating bone defects have been developed rapidly, but we are still facing the fact that it could take a long time of stepping into clinical trial. Prospective pre-clinical studies of these hydrogels/scaffolds are required in the future to further advance their development in

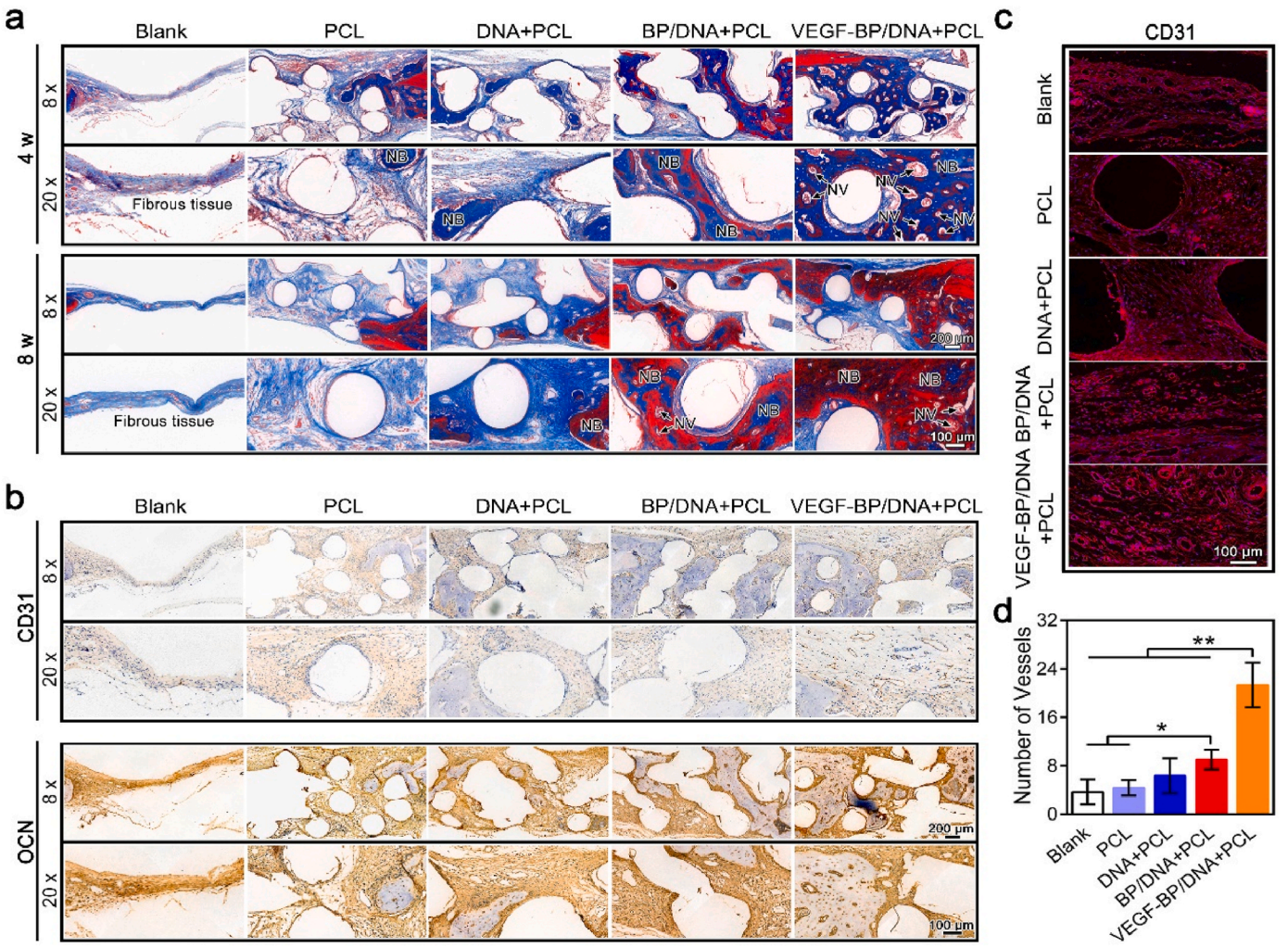

Fig. 9. Expression of matrix and marker proteins in the bone defect after gel-scaffold construct implantation. (a) Masson's trichrome staining images of cranial defects after the implantation of gel-scaffold constructs for 4 and 8 weeks, the NV indicated by the arrow represented for new blood vessels, and NB represented for new bone tissue. (b) OCN and CD31 immunohistochemical staining images of cranial defects after the implantation of gel-scaffold constructs for 4 weeks, the yellow-brown area was the positive expression area of OCN and CD31. (c) CD31 immunofluorescence staining images of cranial defects after the implantation of gel-scaffold constructs for 4 weeks, CD31 was marked in red and the nuclei were marked in blue. (d) Quantitative analysis of newly formed micro-vessels in each group based on CD31 immunofluorescence staining.

the field of bone tissue engineering.

4. Conclusions

In conclusion, we have demonstrated an interesting strategy to endow inert 3D printed PCL scaffold with a dual regulatory effect on angiogenesis and osteogenesis for cranial bone regeneration. Imparting BPNSs into DNA dynamic hydrogel led to the mechanical reinforcement of the reversible network. The integrative nano-enabled gel-scaffold construct exhibited sustained release of VEGF due to the noncovalent interactions between VEGF and BPNSs. The *in vivo* results from a rat cranial defect model demonstrated that the gel-scaffold construct could synergistically promote osteogenesis and the growth of mature blood vessels to achieve enhanced bone regeneration outcomes. Taken together, the advances demonstrated in this study may open new opportunities for the development of promising bioactive construct for bone tissue engineering.

Data availability

The data reported in this manuscript are available upon request.

Ethics approval and consent to participate

All animal experiments were performed in strict accordance with the Guide for the Care and Use of Laboratory Animals (Ministry of Science and Technology of the People's Republic of China, Policy No. 2006398). The animal procedures were performed in accordance with the Guidelines for Care and Use of Laboratory Animals of South China University of Technology and approved by the University Animal Ethics Committee (approval No. 2018005).

CRediT authorship contribution statement

Yali Miao: Data curation, Methodology, Investigation, Writing – original draft. **Yunhua Chen:** Conceptualization, Methodology, Data curation, Writing – review & editing. **Jinshui Luo:** Investigation. **Xiao Liu:** Investigation. **Qian Yang:** Investigation. **Xuetao Shi:** Conceptualization, Writing – review & editing. **Yingjun Wang:** Supervision, Project administration, Funding acquisition.

Declaration of competing interest

The authors have no conflicts to declare.

Acknowledgements

This work was financially supported by the National Key Research and Development Program of China (2018YFA0703000), the National Natural Science Foundation of China (22072047, U1801252), the Science and Technology Program of Guangzhou (202007020002).

References

[1] J. Zhang, H. Eyisoylu, X.H. Qin, M. Rubert, R. Muller, 3D bioprinting of graphene oxide-incorporated cell-laden bone mimicking scaffolds for promoting scaffold fidelity, osteogenic differentiation and mineralization, Acta Biomater. 121 (2021) 637–652, https://doi.org/10.1016/j.actbio.2020.12.026.
[2] J. Zhang, J. Jia, J.P. Kim, H. Shen, F. Yang, Q. Zhang, M. Xu, W. Bi, X. Wang, J. Yang, D. Wu, Ionic colloidal molding as a biomimetic scaffolding strategy for uniform bone tissue regeneration, Adv. Mater. 29 (17) (2017), 1605546, https://doi.org/10.1002/adma.201605546.
[3] B. Clarke, Normal bone anatomy and physiology, Clin. J. Am. Soc. Nephrol. 3 (Suppl 3) (2008) S131–S139, https://doi.org/10.2215/CJN.04151206.
[4] A.C. Daly, F.E. Freeman, T. Gonzalez-Fernandez, S.E. Critchley, J. Nulty, D.J. Kelly, 3D bioprinting for cartilage and osteochondral tissue engineering, Adv. Healthc Mater. 6 (22) (2017), 1700298, https://doi.org/10.1002/adhm.201700298.
[5] Z. Wang, G. An, Y. Zhu, X. Liu, Y. Chen, H. Wu, Y. Wang, X. Shi, C. Mao, 3D-printable self-healing and mechanically reinforced hydrogels with host-guest non-covalent interactions integrated into covalently linked networks, Mater. Horiz. 6 (4) (2019) 733–742, https://doi.org/10.1039/C8MH01208C.
[6] H. Zhao, J. Xu, H. Yuan, E. Zhang, N. Dai, Z. Gao, Y. Huang, F. Lv, L. Liu, Q. Gu, S. Wang, 3D printing of artificial skin patches with bioactive and optically active polymer materials for anti-infection and augmenting wound repair, Mater. Horiz. 9 (1) (2022) 342–349, https://doi.org/10.1039/d1mh00508a.
[7] Y. Lai, Y. Li, H. Cao, J. Long, X. Wang, L. Li, C. Li, Q. Jia, B. Teng, T. Tang, J. Peng, D. Eglin, M. Alini, D.W. Grijpma, G. Richards, L. Qin, Osteogenic magnesium incorporated into PLGA/TCP porous scaffold by 3D printing for repairing challenging bone defect, Biomaterials 197 (2019) 207–219, https://doi.org/10.1016/j.biomaterials.2019.01.013.
[8] Y. Zhang, M. Chen, J. Tian, P. Gu, H. Cao, X. Fan, W. Zhang, In situ bone regeneration enabled by a biodegradable hybrid double-network hydrogel, Biomater. Sci. 7 (8) (2019) 3266–3276, https://doi.org/10.1039/c9bm00561g.
[9] M.J. Dalby, N. Gadegaard, R. Tare, A. Andar, M.O. Riehle, P. Herzyk, C.D. W. Wilkinson, R.O.C. Oreffo, The control of human mesenchymal cell differentiation using nanoscale symmetry and disorder, Nat. Mater. 6 (12) (2007) 997–1003, https://doi.org/10.1038/nmat2013.
[10] H. Zhang, Q. Cai, Y. Zhu, W. Zhu, A simple hydrogel scaffold with injectability, adhesivity and osteogenic activity for bone regeneration, Biomater. Sci. 9 (3) (2021) 960–972, https://doi.org/10.1039/d0bm01840f.
[11] Z. Siddiqui, B. Sarkar, K.K. Kim, A. Kumar, R. Paul, A. Mahajan, J.M. Grasman, J. Yang, V.A. Kumar, Self-assembling peptide hydrogels facilitate vascularization in two-component scaffolds, Chem. Eng. J. 422 (2021), https://doi.org/10.1016/j.cej.2021.130145.
[12] G. Zhu, T. Zhang, M. Chen, K. Yao, X. Huang, B. Zhang, Y. Li, J. Liu, Y. Wang, Z. Zhao, Bone physiological microenvironment and healing mechanism: basis for future bone-tissue engineering scaffolds, Bioact. Mater. 6 (11) (2021) 4110–4140, https://doi.org/10.1016/j.bioactmat.2021.03.043.
[13] M.B. Sordi, A. Cruz, M.C. Fredel, R. Magini, P.T. Sharpe, Three-dimensional bioactive hydrogel-based scaffolds for bone regeneration in implant dentistry, Mater. Sci. Eng. C Mater. Biol. Appl. 124 (2021), 112055, https://doi.org/10.1016/j.msec.2021.112055.
[14] J.D. Kretlow, L. Klouda, A.G. Mikos, Injectable matrices and scaffolds for drug delivery in tissue engineering, Adv. Drug Deliv. Rev. 59 (4–5) (2007) 263–273, https://doi.org/10.1016/j.addr.2007.03.013.
[15] J. Whitehead, K.H. Griffin, M. Gionet-Gonzales, C.E. Vorwald, S.E. Cinque, J. K. Leach, Hydrogel mechanics are a key driver of bone formation by mesenchymal stromal cell spheroids, Biomaterials 269 (2021), https://doi.org/10.1016/j.biomaterials.2020.120607, 120607.
[16] J. Miszuk, Z. Liang, J. Hu, H. Sanyour, Z. Hong, H. Fong, H. Sun, An elastic mineralized 3D electrospun PCL nanofibrous scaffold for drug release and bone tissue engineering, ACS Appl. Bio Mater. 4 (4) (2021) 3639–3648, https://doi.org/10.1021/acsabm.1c00134.
[17] M. Mehrali, A. Thakur, C.P. Pennisi, S. Talebian, A. Arpanaei, M. Nikkhah, A. Dolatshahi-Pirouz, Nanoreinforced hydrogels for tissue engineering: biomaterials that are compatible with load-bearing and electroactive tissues, Adv. Mater. 29 (8) (2017), 1603612, https://doi.org/10.1002/adma.201603612.
[18] C.C. Huang, M. Kang, S. Shirazi, Y. Lu, L.F. Cooper, P. Gajendrareddy, S. Ravindran, 3D Encapsulation and tethering of functionally engineered extracellular vesicles to hydrogels, Acta Biomater. 126 (2021) 199–210, https://doi.org/10.1016/j.actbio.2021.03.030.
[19] A.N. Cho, Y. Jin, Y. An, J. Kim, Y.S. Choi, J.S. Lee, J. Kim, W.Y. Choi, D.J. Koo, W. Yu, G.E. Chang, D.Y. Kim, S.H. Jo, J. Kim, S.Y. Kim, Y.G. Kim, J.Y. Kim, N. Choi, E. Cheong, Y.J. Kim, H.S. Je, H.C. Kang, S.W. Cho, Microfluidic device with brain extracellular matrix promotes structural and functional maturation of human brain organoids, Nat. Commun. 12 (1) (2021) 4730, https://doi.org/10.1038/s41467-021-24775-5.
[20] M. Rizwan, A.E.G. Baker, M.S. Shoichet, Designing hydrogels for 3D cell culture using dynamic covalent crosslinking, Adv. Healthc. Mater. 10 (12) (2021), e2100234, https://doi.org/10.1002/adhm.202100234.
[21] Y. Zhao, Z. Cui, B. Liu, J. Xiang, D. Qiu, Y. Tian, X. Qu, Z. Yang, An injectable strong hydrogel for bone reconstruction, Adv. Healthc. Mater. 8 (17) (2019), e1900709, https://doi.org/10.1002/adhm.201900709.
[22] A.J. Feliciano, C. van Blitterswijk, L. Moroni, M.B. Baker, Realizing tissue integration with supramolecular hydrogels, Acta Biomater. 124 (2021) 1–14, https://doi.org/10.1016/j.actbio.2021.01.034.
[23] K. Zhang, Q. Feng, Z. Fang, L. Gu, L. Bian, Structurally dynamic hydrogels for biomedical applications: pursuing a fine balance between macroscopic stability and microscopic dynamics, Chem. Rev. 121 (2021) 11149–11193, https://doi.org/10.1021/acs.chemrev.1c00071.
[24] X.Y. Dai, Y.Y. Zhang, L.N. Gao, T. Bai, W. Wang, Y.L. Cui, W.G. Liu, A mechanically strong, highly stable, thermoplastic, and self-healable supramolecular polymer hydrogel, Adv. Mater. 27 (23) (2015) 3566–3571, https://doi.org/10.1002/adma.201500534.
[25] J. Mo, Y. Dai, C. Zhang, Y. Zhou, W. Li, Y. Song, C. Wu, Z. Wang, Design of ultra-stretchable, highly adhesive and self-healable hydrogels via tannic acid-enabled dynamic interactions, Mater. Horiz. 8 (12) (2021) 3409–3416, https://doi.org/10.1039/d1mh01324f.
[26] P.K. Lo, P. Karam, F.A. Aldaye, C.K. McLaughlin, G.D. Hamblin, G. Cosa, H. F. Sleiman, Loading and selective release of cargo in DNA nanotubes with longitudinal variation, Nat. Chem. 2 (4) (2010) 319–328, https://doi.org/10.1038/Nchem.575.
[27] S. Basu, S. Pacelli, Y. Feng, Q. Lu, J. Wang, A. Paul, Harnessing the noncovalent interactions of DNA backbone with 2D silicate nanodisks to fabricate injectable therapeutic hydrogels, ACS Nano 12 (10) (2018) 9866–9880, https://doi.org/10.1021/acsnano.8b02434.
[28] W. Pan, C. Dai, Y. Li, Y. Yin, L. Gong, J.O. Machuki, Y. Yang, S. Qiu, K. Guo, F. Gao, PRP-chitosan thermoresponsive hydrogel combined with black phosphorus nanosheets as injectable biomaterial for biotherapy and phototherapy treatment of rheumatoid arthritis, Biomaterials 239 (2020), 119851, https://doi.org/10.1016/j.biomaterials.2020.119851.
[29] J. Shao, C. Ruan, H. Xie, P.K. Chu, X.F. Yu, Photochemical activity of black phosphorus for near-infrared light controlled in situ biomineralization, Adv. Sci. 7 (14) (2020), https://doi.org/10.1002/advs.202000439, 2000439.
[30] Z. Wang, J. Zhao, W. Tang, L. Hu, X. Chen, Y. Su, C. Zou, J. Wang, W.W. Lu, W. Zhen, R. Zhang, D. Yang, S. Peng, Multifunctional nanoengineered hydrogels consisting of black phosphorus nanosheets upregulate bone formation, Small 15 (41) (2019), e1901560, https://doi.org/10.1002/smll.201901560.
[31] L. Peng, N. Abbasi, Y. Xiao, Z.J. Xie, Black phosphorus: degradation mechanism, passivation method, and application for in situ tissue regeneration, Adv. Mater. Interfac. 7 (23) (2020), https://doi.org/10.1002/admi.202001538, 2001538.
[32] L. Tong, Q. Liao, Y. Zhao, H. Huang, A. Gao, W. Zhang, X. Gao, W. Wei, M. Guan, P. K. Chu, H. Wang, Near-infrared light control of bone regeneration with biodegradable photothermal osteoimplant, Biomaterials 193 (2019) 1–11, https://doi.org/10.1016/j.biomaterials.2018.12.008.
[33] S.M. Chim, J. Tickner, S.T. Chow, V. Kuek, B. Guo, G. Zhang, V. Rosen, W. Erber, J. Xu, Angiogenic factors in bone local environment, Cytokine Growth Factor Rev. 24 (3) (2013) 297–310, https://doi.org/10.1016/j.cytogfr.2013.03.008.
[34] M.L. Brandi, P. Collin-Osdoby, Vascular biology and the skeleton, J. Bone Miner. Res. 21 (2) (2006) 183–192, https://doi.org/10.1359/JBMR.050917.
[35] J. Zhou, Z. Li, M. Ying, M. Liu, X. Wang, X. Wang, L. Cao, H. Zhang, G. Xu, Black phosphorus nanosheets for rapid microRNA detection, Nanoscale 10 (11) (2018) 5060–5064, https://doi.org/10.1039/c7nr08900g.
[36] X. Zeng, M. Luo, G. Liu, X. Wang, W. Tao, Y. Lin, X. Ji, L. Nie, L. Mei, Polydopamine-modified black phosphorous nanocapsule with enhanced stability and photothermal performance for tumor multimodal treatments, Adv. Sci. 5 (10) (2018), 1800510, https://doi.org/10.1002/advs.201800510.
[37] W. Chen, J. Ouyang, H. Liu, M. Chen, K. Zeng, J. Sheng, Z. Liu, Y. Han, L. Wang, J. Li, L. Deng, Y.N. Liu, S. Guo, Black phosphorus nanosheet-based drug delivery system for synergistic photodynamic/photothermal/chemotherapy of cancer, Adv. Mater. 29 (5) (2017), 1603864, https://doi.org/10.1002/adma.201603864.
[38] H. Wang, X.-F. Yu, Few-layered black phosphorus: from fabrication and customization to biomedical applications, Small 14 (6) (2018), 1702830, https://doi.org/10.1002/smll.201702830.
[39] W. Tao, X.B. Zhu, X.H. Yu, X.W. Zeng, Q.L. Xiao, X.D. Zhang, X.Y. Ji, X.S. Wang, J. J. Shi, H. Zhang, L. Mei, Black phosphorus nanosheets as a robust delivery platform for cancer theranostics, Adv. Mater. 29 (1) (2017), 1603276, https://doi.org/10.1002/adma.201603276.
[40] W.H. Li, J.J. Wu, L. Wu, B.D. Zhang, H.G. Hu, L. Zhao, Z.B. Li, X.F. Yu, Y.M. Li, Black phosphorous nanosheet: a novel immune-potentiating nanoadjuvant for near-infrared-improved immunotherapy, Biomaterials 273 (2021), https://doi.org/10.1016/j.biomaterials.2021.120788, 120788.
[41] Z. Li, G. Luo, W.P. Hu, J.L. Hua, S. Geng, P.K. Chu, J. Zhang, H. Wang, X.F. Yu, Mediated drug release from nanovehicles by black phosphorus quantum dots for efficient therapy of chronic obstructive pulmonary disease, Angew. Chem. Int. Ed. 59 (46) (2020) 20568–20576, https://doi.org/10.1002/anie.202008379.
[42] M. Crombez, P. Chevallier, R.C. Gaudreault, E. Petitclerc, D. Mantovani, G. Laroche, Improving arterial prosthesis neo-endothelialization: application of a proactive VEGF construct onto PTFE surfaces, Biomaterials 26 (35) (2005) 7402–7409, https://doi.org/10.1016/j.biomaterials.2005.05.051.
[43] V. Tayari, N. Hemsworth, I. Fakih, A. Favron, E. Gaufres, G. Gervais, R. Martel, T. Szkopek, Two-dimensional magnetotransport in a black phosphorus naked

quantum well, Nat. Commun. 6 (2015) 7702, https://doi.org/10.1038/ncomms8702.

[44] Y. Arima, H. Iwata, Effect of wettability and surface functional groups on protein adsorption and cell adhesion using well-defined mixed self-assembled monolayers, Biomaterials 28 (20) (2007) 3074–3082, https://doi.org/10.1016/j.biomaterials.2007.03.013.

[45] G. Zhong, J. Yao, X. Huang, Y. Luo, M. Wang, J. Han, F. Chen, Y. Yu, Injectable ECM hydrogel for delivery of BMSCs enabled full-thickness meniscus repair in an orthotopic rat model, Bioact. Mater. 5 (4) (2020) 871–879, https://doi.org/10.1016/j.bioactmat.2020.06.008.

[46] P. Qiu, M. Li, K. Chen, B. Fang, P. Chen, Z. Tang, X. Lin, S. Fan, Periosteal matrix-derived hydrogel promotes bone repair through an early immune regulation coupled with enhanced angio- and osteogenesis, Biomaterials 227 (2020), 119552, https://doi.org/10.1016/j.biomaterials.2019.119552.